JOURNAL OF GEOPHYSICAL RESEARCH, VOL. 107, NO. A4, 10.1029/2001JA900122, 2002

A new perspective on plasma supply mechanisms to the magnetotail from a statistical comparison of dayside mirroring O^+ at low altitudes with lobe/mantle beams

K. Seki,[1,2] R. C. Elphic,[1] M. F. Thomsen,[1] J. Bonnell,[3] J. P. McFadden,[3]
E. J. Lund,[4] M. Hirahara,[5] T. Terasawa,[6] and T. Mukai[7]

Received 4 April 2001; revised 17 August 2001; accepted 17 August 2001; published 30 April 2002

[1] Observations of tailward cold O^+ beams (COBs) in the distant lobe/mantle shed new light upon plasma supply mechanisms to the magnetotail since their location up to a tailward distance of 210 R_E is not explicable with a conventional view of magnetospheric dynamics. The COBs exist primarily in the mantlelike regions that correspond to the transport route of magnetic flux tubes reconnected at the dayside magnetopause, and thus it has been suggested that these high-energy COBs in the distant lobe/mantle have originated from trapped O^+ ions in the dayside magnetosphere. In order to examine the validity of this scenario the phase space density (PSD) of the COBs observed by Geotail is compared statistically with that of mirroring O^+ ions around the cusp observed by FAST at low altitudes (400–4200 km) utilizing particle trajectory tracings in empirical magnetospheric models. The energy distribution of the averaged peak PSD of COBs is different at energies below and above ~1 keV and thus suggests that more than one source contributes to the COBs. The mirroring O^+ increases in quantity with increasing solar activity and suggest increment of trapped O^+ ions in the dayside magnetosphere. A statistical comparison shows that the O^+ PSD around the low-altitude cusp is similar to that of COBs above ~1 keV, while the COB PSD is typically higher than that of O^+ at FAST at energies <~1 keV. These results suggest that the trapped O^+ in the dayside magnetosphere is a potential source of COBs at energies above 1 keV, while for COBs below 1 keV, polar O^+ outflows from the cusp/cleft regions are the most probable source, as suggested by a conventional view. *INDEX TERMS:* 2740 Magnetospheric Physics: Magnetospheric configuration and dynamics; 2744 Magnetospheric Physics: Magnetotail; 2736 Magnetospheric Physics: Magnetosphere/ionosphere interactions; *KEYWORDS:* magnetotail O^+ beams, dayside magnetosphere, trapped ionospheric ions, FAST, GEOTAIL, lobe/mantle

1. Introduction

[2] It is well known that a variety of particles precipitate into the Earth's ionosphere via a variety of processes [*Lyons*, 1997; *Newell and Meng*, 1988, 1992; *Sergeev et al.*, 1997; *Woch and Lundin*, 1992, and references therein]. Precipitation of magnetosheath particles can be seen in the open field line regions where one side of a magnetic field line is connected to the solar wind and another side is connected to the ionosphere, i.e., in the polar regions such Mas the cusp/cleft, plasma mantle, and lobe. These particles correspond to the loss cone part of the magnetosheath distribution that has entered the magnetosphere through field lines crossing the magnetopause. In the high-latitude portion of the polar cap, few ions are observed, while uniform electron precipitation called polar rain is observed within the entire polar cap predominantly in the Northern (Southern) Hemisphere during negative (positive) interplanetary magnetic field (IMF) B_x periods [*Winningham and Heikkila*, 1974; *Gussenhoven et al.*, 1984]. Within the dayside polar cap at lower latitudes near the magnetic separatrix (the boundary between open and closed magnetic field lines), enhanced fluxes of both electrons and ions can be seen. The enhanced electron flux occurs at energies below ~100 eV, while the enhanced ion flux extends to above 1 keV near the separatrix and the ion energy decreases with increasing magnetic latitude. This energy-latitude dispersion is considered to be a result of a time-of-flight effect caused by poleward/tailward convection of the reconnected field lines and a finite-sized entry region [*Onsager et al.*, 1993]. The equatorward portion of this region of dispersed ion precipitation is referred to as the cusp. The poleward portion of the dispersion region is referred as the mantle, and it continues to the lobe region where little ion precipitation is observed.

[3] In the regions equatorward of the polar caps, on the other hand, magnetospheric particles trapped on closed field lines are precipitating to the ionosphere. The precipitation in the closed region is considered to be caused by pitch angle scattering, and

---

[1] Space and Atmospheric Sciences Group (NIS-1), Los Alamos National Laboratory, Los Alamos, New Mexico, USA.

[2] Now at Integrated Studies Division, Solar Terrestrial Environment Laboratory, Nagoya University, Toyokawa, Japan.

[3] Space Science Laboratory, University of California, Berkeley, California, USA.

[4] Space Science Center, University of New Hampshire, Durham, New Hampshire, USA.

[5] Department of Physics, College of Science, Rikkyo University, Tokyo, Japan.

[6] Department of Earth and Planetary Science, Graduate School of Science, University of Tokyo, Tokyo, Japan.

[7] Institute of Space and Astronautical Science, Kanagawa, Japan.

0148-0227/02/JA900122$09.00

many scattering processes such as nonguiding center motion in the weak magnetic field regions, field-aligned acceleration by parallel electric fields, and scattering by plasma waves have been proposed [*Cowley*, 1980; *Lyons and Speiser*, 1982; *Speiser*, 1984; *Büchner and Zelenyi*, 1989; *Delcourt et al.*, 1996; *Sergeev et al.*, 1997]. Observationally, the plasma sheet precipitation has broad energy spectra with significant fluxes extending typically up to several keV for electrons and to a few hundreds of keV for ions. The temperature in the plasma sheet is, however, highly variable with the solar wind conditions and tends to increase when the IMF is southward [*Terasawa et al.*, 1997]. Since particles may enter the plasma sheet from the mantle, low-latitude boundary layer, and ionospheric outflows, both the ionospheric and solar wind plasmas are considered to contribute to the precipitation in closed field line regions. One possible way to distinguish these two sources is to investigate the ratio of respective heavy ion species, which exist only in the ionosphere (O^+, He^+) or the solar wind (He^{++}).

[4] From in situ observations of the trapped particles in the dayside magnetosphere it is known that the ionospheric ion population (especially O^+) has a strong dependence on the solar EUV flux as inferred from $F_{10.7}$ and increases with the solar activity [*Young et al.*, 1982]. It is also known that the flux of the polar ionospheric O^+ outflows increases dramatically with $F_{10.7}$ [*Yau and André*, 1997, and references therein]. Therefore the quantity of trapped O^+ ions in the magnetosphere is expected to increase with increasing $F_{10.7}$, and the solar activity dependence needs to be taken into account for investigation of their properties.

[5] A knowledge of the quantitative properties of the trapped O^+ is crucial to discussions of the supply mechanisms of cold O^+ beams (COBs) in the tail lobe/mantle. Observations of COBs over a wide range of distances in the lobe/mantle regions [*Hirahara et al.*, 1998; *Seki et al.*, 1996, 1998a, 2000a] cannot be explained with a conventional view of plasma supply mechanisms to the magnetotail, i.e., plasma supply from polar ionospheric outflows on their way to the plasma sheet because of magnetospheric convection. On the basis of statistical properties of COBs, three probable supply scenarios of the COBs are proposed by *Seki et al.* [1998a]. Among the three candidates ((1) extra energization of dayside polar ionospheric outflows; (2) circulation of energetic upward flowing ion (UFI) beams generated mainly around the nightside auroral zone, and (3) release of trapped ions in the dayside magnetosphere by the dayside reconnection) the second and third require an adequate trapped O^+ ion population in the dayside magnetosphere so as to be a main contributor to COBs. In order to examine the validity of these candidate supply scenarios the phase space densities (PSDs) of COBs are compared with those of mirroring O^+ at low altitudes in accordance with Liouville's theorem for an event in our previous study [*Seki et al.*, 2000b]. The result suggests that O^+ precipitation in closed field line regions is adequate in quantity to supply COBs under the assumption that there is no acceleration/deceleration during the transport and that the PSD of mirroring O^+ in open regions is typically smaller than but sometimes comparable to that of COBs. Since it was only an event study, statistical comparison is also needed.

[6] In this study we will investigate the quantitative properties of the trapped O^+ ions in the dayside magnetosphere statistically, with the goal of discussing the supply mechanisms of COBs observed by Geotail in the lobe/mantle regions. Data of the FAST satellite, which have enough sensitivity and time resolution to detect the precipitating and mirroring O^+ ions at low altitudes, are used for two time intervals in the low and high solar activity periods. For comparison, we take account of the minimum energy gain from FAST to Geotail estimated with trajectory tracing of O^+ ions in empirical magnetospheric models (the Tsyganenko 1996 magnetic field model [*Tsyganenko and Stern*, 1996] and the Weimer 1996 [*Weimer*, 1995, 1996] + corotation electric potential model). On the basis of the obtained results, plasma supply mechanisms to the lobe/mantle regions are reconsidered in section 5.

2. Instrumentation

[7] The Geotail spacecraft was launched on 24 July 1992. The low-energy particle (LEP) instrument onboard Geotail measures ions with energies from 32 eV/q to 39 keV/q. There are two data acquisition modes in the LEP. In the three-dimensional (3-D) mode, fully 3-D distribution functions $f(v)$ are obtained for 8 hours a day on average. In the 2-D mode, 2-D quasi-equatorial projections of the original $f(v)$ and their onboard 3-D moments (density, velocity, and pressure tensor) are obtained with a full time coverage [*Mukai et al.*, 1994a]. For statistics we used the 2-D mode data in order to increase the number of events. It is confirmed with time intervals that have both the 2-D and 3-D data that these two data give reasonably similar phase space densities. The magnetic field (MGF) instrument provides the 3-D magnetic field data [*Kokubun et al.*, 1994]. Both the plasma and MGF data used here have a time resolution of 12 s.

[8] The FAST satellite was launched into a 4180 × 350 km, 82.9° inclination orbit on 21 August 1996 [*Carlson et al.*, 1998]. Technical details of the electrostatic analyzers (ESAs) and the time-of-flight energy angle mass spectrometer (TEAMS) onboard FAST are given by *Carlson and McFadden* [1998] and *Möbius et al.* [1998], respectively. The ESAs measure full pitch angle distributions of electrons (4 eV to 30 keV) and ions (3 eV to 25 keV) with a time resolution as good as 78 ms. TEAMS can determine the energy, mass per charge, and incoming direction of ions over an energy range of 1 eV to 12 keV and measure 3-D distribution of each ion species with time resolution down to half a spacecraft spin ($\sim$2.5 s). If there is an intense flux of H^+, there can be some contamination to higher m^{-1}/q bins in TEAMS. All data points in which the proton contamination to O^+ is above 50% are excluded from the analysis.

[9] It is known that TEAMS sometimes has trouble with onboard data accumulation and that the pitch angle distributions at certain energies are not reliable. (This accumulation problem does not cause any error in the omnidirectional energy-time spectrogram.) In order to remove the problem we have corrected TEAMS data assuming that the four major ion species (H^+, He^{++}, He^+, and O^+) have the same pitch angle distribution as that observed by the ion electrostatic analyzers (IESAs) at each energy bin. It is confirmed that the error due to this accumulation problem is negligible in this specific PSD comparison with Geotail (see *Seki et al.* [2000b] for more details). However, it should be noted that the O^+ PSDs can contain an error of $\sim$40–50% due to the low count rate typically in the open field line regions, and the error becomes smaller in the higher count rate regions.

3. Estimation of Minimum Energy Gain From FAST to Geotail

[10] In this section we estimate the possible energy gain from the FAST to the Geotail location. For estimation, trajectories of O^+ ions launched from the low-altitude dayside polar regions are traced in empirical magnetospheric MGF and convection models to the region of $X_{GSM} = -20R_E$.

3.1. Model and Code Description

[11] We used two empirical models, i.e. the Tsvganenko 1996 (T96) model for the MGF [*Tsyganenko and Stern*, 1996, and references therein] and the Weimer 1996 (W96) model for electric potential [*Weimer*, 1995, 1996] to calculate the electric field. The T96 model is the last released version (22 June 1996) of a new data-based model of the geomagnetospheric MGF with an explicitly defined realistic magnetopause, large-scale region 1 and 2

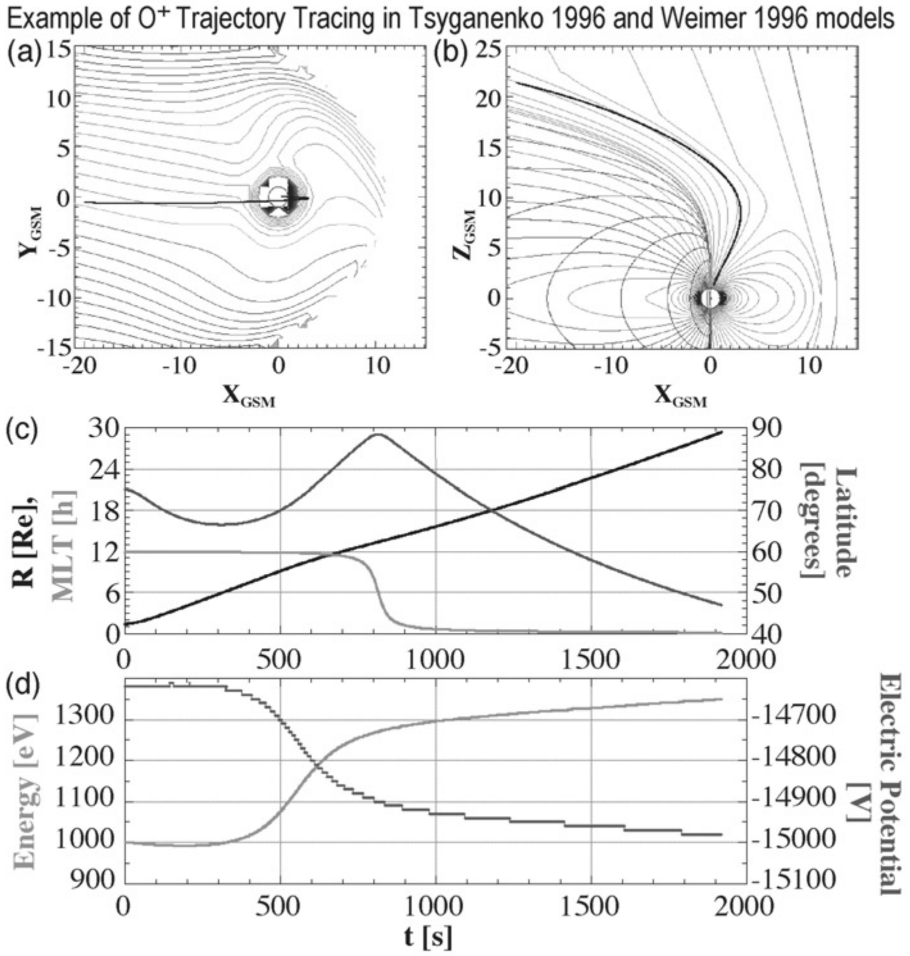

Figure 1. An example of O^+ trajectory in steady empirical magnetospheric models: T96 magnetic field and W96 electric potential models are displayed in GSM coordinates with tilt angle assumed to be zero. Input parameters to the models are dynamic pressure of the solar wind, 2 nPa; the *Dst* index, -100; IMF B_y, 0 nT; IMF B_z; -5 nT; and solar wind velocity, 450 km s^{-1}. (a) The colored lines in panel display electric equipotential lines for each 2.5 kV mapped with T96 model to the equatorial plane. (b) The magnetic fields that have their foot points at MLT = 0, 6, or 12 hours are displayed with colored lines. In each panel the traced O^+ trajectory is shown with the black line. (c) Time variation of particle position with the geocentric distance R (black), the MLT (blue), and the latitude (red). The scales for R and MLT are the same and are shown on the left-hand side of the panel. (d) The O^+ energy (blue) and local electric potential at the particle position (red). See color version of this figure at back of this issue.

Birkeland current systems, and IMF penetration across the boundary. Input parameters of T96 are solar wind pressure, *Dst* index, B_y and B_z components of IMF, geodipole tilt angle, and GSM position of the observation point (X, Y, Z). As a rough estimate, the parameter values should remain within these intervals: P_{dyn} between 0.5 and 10 nPa, *Dst* between -100 and +20, and IMF B_y and IMF B_z between -10 and +10 nT. The only parameter that controls the size of the model magnetopause is the solar wind ram pressure P_{dyn}. For details on the approach used in devising this model we would like to refer readers to the literature [*Tsyganenko and Peredo*, 1994; *Fairfield et al.*, 1994; *Tsyganenko*, 1995; *Tsyganenko and Stern*, 1996]

[12] The W96 model has been developed to derive the electric potentials in the high-latitude ionosphere resulting from any arbitrary combination of IMF magnitude and orientation, solar wind velocity, and dipole tilt angle. This model is based on spherical harmonic coefficients that were derived by a least error fit of the double-probe electric field measurements by the DE 2 satellite, using all polar cap passes during which there were IMF data available from the ISEE 3 or IMP 8 satellites. The data used to derived the W96 model had group-averaged IMF magnitudes up to 11 nT. Detailed explanations of the model are given by *Weimer* [1995, 1996].

[13] The W96 model can only reproduce the electric potential at high latitudes. In the low-latitude regions the corotation electric field becomes important. To take account of the corotation electric field, we have added the corotational electric potential to the W96 model. The corotational electric potential Φ_c in the form of $\Phi_c = -(M\Omega\cos^2\theta)/R_i$ is used, where M, Ω, and R_i represent the magnetic moments of the Earth's dipole, the angular velocity of the Earth's rotation, and the radial distance from the center of Earth to ionospheric altitude, respectively. In the derivation of Φ_c it is assumed that the MGF is close to the dipole field in the regions where the corotation is important and that the tilt of the dipole and spin axes is zero.

[14] By solving the equation of motion for an O^+ ion,

$$m_{o^+}\frac{dv}{dt} = q_{o^+}(\mathbf{E} + \upsilon \times \mathbf{B}) + \mathbf{F}_g, \qquad (1)$$

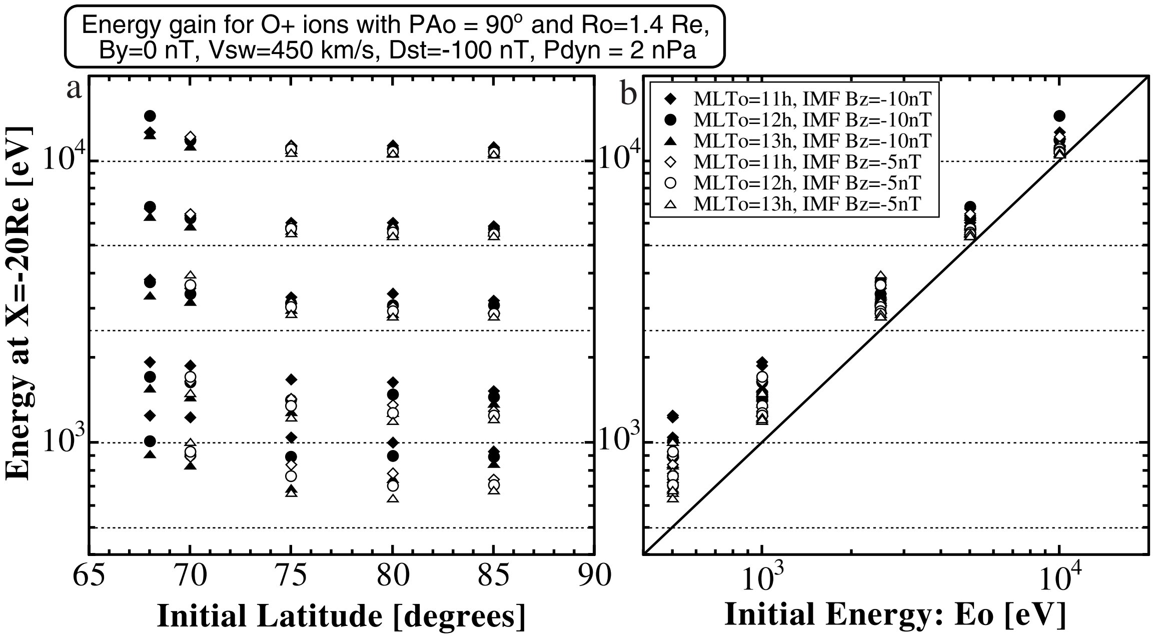

Figure 2. The energy increases from the initial position around the cusp to the lobe/mantle of $X_{\mathrm{GSM}} = -20\ R_E$ are plotted against the initial ILAT and initial energy.

the particle motion is traced in the magnetosphere using the T96 magnetic field model and W96 + corotation electric potential explained above. As shown in (1), the gravitational force of the Earth, $\mathbf{F}_g$, is also taken into account in the calculations. For calculations of the electric field **E**, four points forming a square whose two diagonal lines cross each other at the current particle position are selected on a plane perpendicular to the local MGF. Assuming that the MGF line is an equipotential, we calculate the electric potential at the four points by tracing the MGF line from each selected point to the ionosphere and then the electric field by taking differences of these potential values. Using these values of the electric field and the MGF, we solve (1) with the fourth-order Runge-Kutta method. The code was confirmed to work appropriately with test calculations such as reproduction of the convection motion of low-energy (~1 eV) particles, comparison with results of guiding center approximation, and energy conservation within high-κ (the square root of the ratio of the minimum curvature radius to maximum Larmor radius) regions.

[15] Since the geodipole tilt strengthens the field line curvature in one hemisphere and weakens it in the other, the average energy gain is expected to be close to the one with zero tilt angle. In the trajectory tracing reported in this paper the tilt angle is assumed to be zero for simplicity. The tilt angle change during the typical O^+ travel time from FAST to Geotail is <1°, and effects of time variation are ignored. In the following calculations we use a typical set of input parameters during southward IMF periods to the T96 and W96 models: Dynamic pressure of the solar wind, 2 nPa; the *Dst* index, 100; IMF B_y, 0 nT; and solar wind velocity 450 km^{-1}/s. Two cases of IMF B_z, −5 and −10 nT, are investigated.

3.2. Results of Trajectory Tracing

[16] Figure 1 shows an example of O^+ trajectory tracing in the T96 and W96 models with corotation. As input parameters to the models, typical solar wind parameters in geomagnetically active periods are used, and the IMF is assumed to be purely southward, as mentioned in section 3.1. The color lines in Figure 1a display electric equipotential lines mapped with the T96 model to the equatorial plane. In Figure 1b the MGF lines with footprints at magnetic local time (MLT) = 0, 6, or 12 hours are displayed with color lines. The black line in each panel displays the O^+ trajectory traced in the models, with the O^+ ion initially having an energy of 1 keV and a pitch angle of 90° and being placed in the dayside flux tube at the invariant latitude (ILAT) of 75° and the typical FAST altitude (2550 km). The initial flux tube is connected to the dayside magnetosphere near the separatrix. Then the particle is gradually accelerated upward along the field line by the mirror force and transported to the lobe/mantle regions by the convection electric field.

[17] As shown with blue in Figure 1d, the particle gains energy by 350 eV as it is transported to the magnetotail of $X_{\mathrm{GSM}} = -20\ R_E$. This energy gain is due to the motion across the flux tube to the low electric potential region, and it is consistent with the correspondent decrease in the electric potential shown with the red line. When we compare the properties of the energy increase with the position shown in Figures 1b and 1c, we can see that the energy gain

Table 1. Estimation of Energy Gain (E_{gain}) From FAST to Geotail With O^+ Trajectory Tracing in the T96/W96 Model

Initial Energy, keV	IMF $B_z = -5$ nT		IMF $B_z = -10$ nT	
	minimum E_{gain}, eV	maximum E_{gain}, eV	minimum E_{gain}, eV	maximum E_{gain} eV
0.5	138	511	191	748
1.0	194	710	281	934
2.5	307	1447	370	1300
5.0	426	1489	515	1881
10.0	590	2200	720	4450

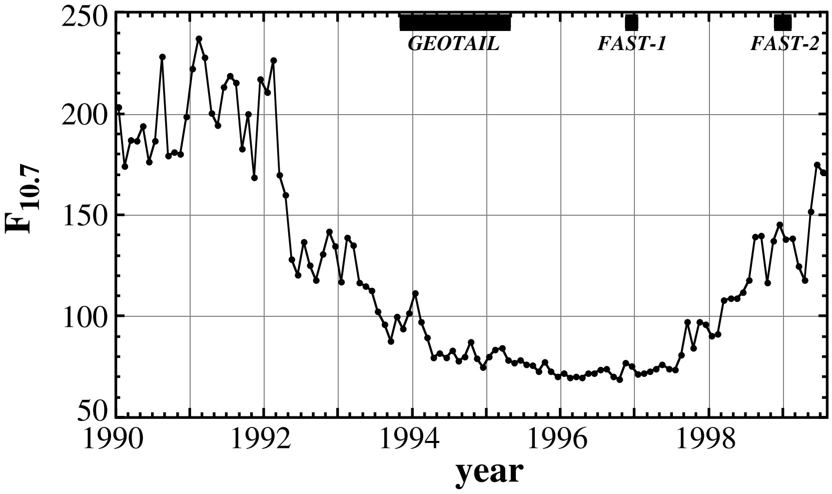

Figure 3. Time variation of monthly average of solar radio fluxes at λ =10.7 cm from January 1990 to June 1999. The flux values are in units of 10^{-22} J s^{-1} m^{-2} Hz^{-1}. Time intervals corresponding to three data sets used in statistical analyses are indicated by black bars on the upper portion of the panel. Descriptions of each data set (GEOTAIL, FAST-1, and FAST-2) are given in the text.

primarily takes place in the region where the field line curvature is large. Thus the curvature drift of the particle is responsible for the motion across the field line and for the energy gain.

[18] Since the extent of the energy gain can vary with the initial energy and position of O^+ ions, next we investigate its variation with ILAT and MLT in terms of five initial energies: 0.5, 1, 2.5, 5, and 10 keV, which are to be used for the comparison of the FAST and Geotail data in section 4. Figure 2 displays the results of trajectory tracings similar to the example shown in Figure 1. As shown in Figure 2a, O^+ ions launched from the low latitudes tend to get more energy than ions from the polar cap. Figure 2b, showing the initial energy dependence, indicates that the absolute value of energy gain increases with initial energy, while the relative importance of the energy gain due to the field line curvature becomes small for high-energy particles. The energy gain also depends on the magnitude of IMF B_z as displayed in Table 1, which shows the minimum and maximum energy gains for each initial energy. This IMF B_z dependence is consistent with enhancement in the magnetospheric convection during the periods of strong southward IMF. In section 13 the estimated minimum energy gain from FAST to Geotail rather than the average is utilized so as to avoid overestimation of importance of the trapped ions in the dayside magnetosphere.

4. Statistical Comparison of FAST and Geotail Data

[19] In this section we will report on statistical comparisons between COBs in the lobe/mantle and mirroring O^+ at low altitudes in the dayside polar magnetosphere on the basis of data from Geotail and FAST. As mentioned in section 1, the main purpose of this comparison is to examine whether the magnetospheric O^+ trapped in the closed field line regions can be a main contributor to the COBs or not. The idea of comparison is similar to that used in our previous study for an event [*Seki et al.*, 2000b] in which the O^+ PSD at the same energies is compared quantitatively according to Liouville's theorem. In this paper we improve the comparison method by taking account of the possible energy gain due to the MGF curvature in the magnetosphere as estimated in section 3. Namely, we assume that the mirroring O^+ ions at FAST altitudes have undergone no energization on their way to the lobe/mantle except for this energy gain due to the steady drift motion in the magnetosphere and that their pitch angles have changed because of the difference of the MGF intensity between the two regions.

[20] As for the COB data set, Geotail data obtained from 5 October 1993 to 31 March 1995 are used, which correspond to the deep tail survey phase of the Geotail mission. Figure 3 shows the time variation of monthly average of the solar radio flux at the wavelength of 10.7 cm $F_{10.7}$ from January 1990 to July 1999. The solar EUV flux increases with the number and size of the active regions on the solar disc, and the $F_{10.7}$ index has been used as a measure of the solar EUV activity [*Young et al.*, 1982]. The time interval corresponding to the COB data set is indicated by a black bar noted as Geotail in Figure 3. As shown, the solar activity is gradually decreasing during this period, and the variation range of $F_{10.7}$ is 74.8–111.3 with an average of 86.9.

[21] Unfortunately, FAST was not yet launched during this period of Geotail's deep tail survey, and as an alternative, we selected two intervals similar to one another except for differences in the solar activity to investigate the properties of trapped O^+ ions in the magnetosphere. These two data sets (herein after referred as FAST-1 and FAST-2) will provide the lower and upper limits of the solar activity dependence of the mirroring ions at low altitudes for comparison. The selected periods are indicated in Figure 3 with black bars noted as FAST-1 and FAST-2. The FAST-1 data set contains 326 crossings across the northern polar regions from 15 November 1996 to 11 January 1997, and it corresponds to the low solar activity whose $F_{10.7}$ range is 71.6–76.9 with an average of 74.6. On the other hand, the FAST-2 data set consists of 178 northern polar crossings from 14 November 1998 to 13 February 1999 and corresponds to higher solar activity whose $F_{10.7}$ range is 137.1–145.5 with an average of 139.8. In the following, PSDs of COBs are compared statistically with those of mirroring O^+ in the dayside polar regions using these three data sets: Geotail, FAST-1, and FAST-2.

4.1. Geotail Observations

[22] We have selected COB events observed during an 18 month period from October 1993 to March 1995 to calculate PSD of COBs. A detailed explanation for the event selection is given by *Seki et al.* [1998a]. For each 12 s of data in the data set the peak PSD of the O^+ beam is saved with energy at which the peak is detected. Figure 4a shows the energy distribution of the peak of

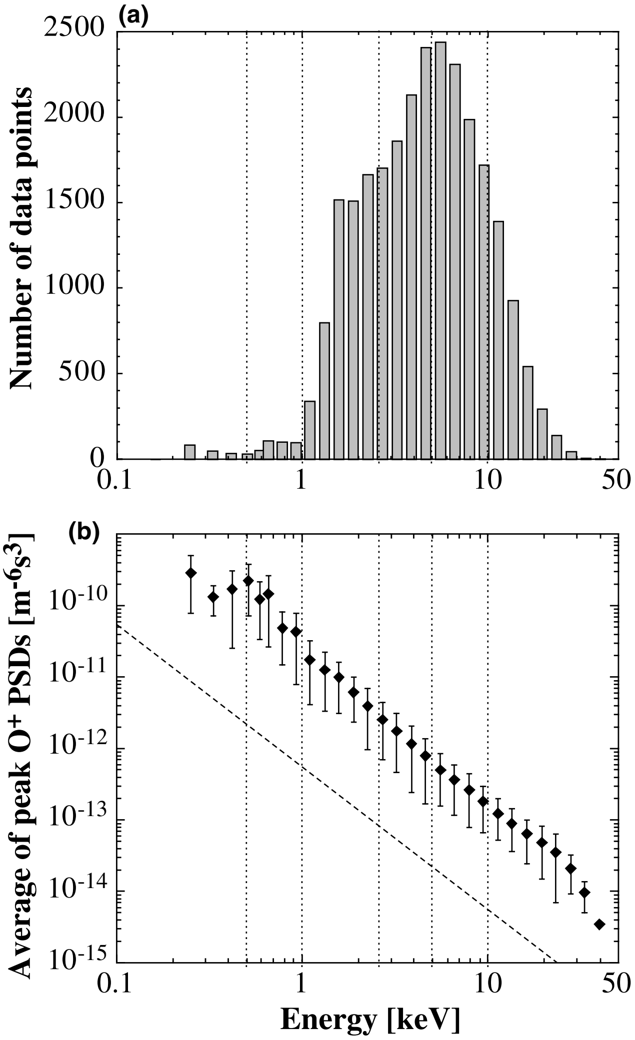

Figure 4. Distribution of peak PSD (phase space density) of COBs observed by Geotail from October 1993 to March 1995. (a) Histogram of the energy at which peak PSD is observed. Each energy range of the histogram corresponds to the energy range of an energy bin of Geotail LEP instruments. (b) Average of the peak PSDs in each energy range of Figure 4a is plotted against the central energy of the each bin with error bars showing the standard deviation. The dashed line displays the one-count level of the instrument. The vertical dotted lines indicate the five energies used for comparison with FAST data.

COBs. Each bin of the histogram corresponds to an energy bin of the Low Energy Particle instrument/Energy-per-charge Analyzer for ions (LEP/EAi) instrument onboard Geotail. As shown, most COBs have a peak at energies above 1 keV, and their typical energy is 2–10 keV. However, this bias toward higher energies does not necessarily mean that the low-energy O$^+$ beams are uncommon in the magnetotail since Geotail does not frequently enter the lobe/mantle regions in the near-Earth tail. Because of this limitation of the Geotail orbit, the data used here are primarily observed in the middle or distant tail where slow ions have already descended into the plasma sheet and only fast ions can remain in the lobe/mantle because of the velocity filter effect due to the $\mathbf{E} \times \mathbf{B}$ convection toward the plasma sheet [*Mukai et al.*, 1994b].

[23] The peak PSDs in each energy range are averaged and plotted against energy with the standard deviations σ_s in Figure 4b. In the energy range from 1 to ~20 keV the distribution decreases monotonically. In this energy range the slope of the average peak PSDs is only a little steeper than that of the instrumental one-count level (dashed line), and this feature comes from a slight decrease in peak counts of COBs with increasing energy. At the energy of ~20–30 keV we see the energy cutoff of the COBs, which is consistent of the results of trajectory tracings from the dayside magnetosphere to the magnetotail in empirical magnetospheric models (Seki et al., manuscript in preparation, 2002). On the other hand, the average peak PSDs in the energy range below 1 keV are larger than PSD values expected from the slope of the high-energy part. Although we cannot confirm the difference because of the small number of observations below 1 keV, this feature might indicate the contribution of more than one source of the COBs: the low-energy part of COBs is mainly contributed by a source that has its typical energy around 500 eV, while the high-energy part is likely to have a hotter source that contains O$^+$ ions in a wide range of energy. The boundary of these two sources is around 1 keV.

4.2. FAST Observations

[24] As mentioned in section 4.1, two time intervals, FAST-1 (low solar activity) and FAST-2 (high solar activity), are selected to investigate properties of O$^+$ ions trapped in the dayside magnetosphere. For comparison with Geotail data we selected five energies, i.e., 0.5, 1, 2.5, 5, and 10 keV, which are indicated by vertical dotted lines in Figure 4. Since the trapped ions observed at FAST altitudes are quite isotropic except for the loss cone [see *Seki et al.*, 2000b, Plate 4], we used all counts in the pitch angle of $\alpha = 90 \pm \theta$, where $\theta = 90° - (\alpha_{\text{loss cone of model field}} + 20)°$, in order to improve count statistics. At FAST altitudes, θ is typically ~30°. FAST observations correspond to the pitch angle range of a few degrees around 0° or 180° in equatorial regions due to difference in **B** field strength. Thus the degree of the contribution of the mirroring component at FAST out of the whole trapped O$^+$ ions in the dayside magnetosphere depends of the distribution in equatorial regions. If the distribution at the equator is almost isotropic, PDSs at FAST altitudes are a good representative of trapped ions. On the other hand, if the distribution has a strong temperature anisotropy of $T_\parallel > T_\perp$ ($T_\parallel < T_\perp$) at the equator, PSDs at FAST altitudes are expected to be larger (smaller) than the average of trapped ions. Therefore the PSD comparison between FAST and GEOTAIL presented in this paper assumes that the distribution of trapped ions in the dayside magnetosphere is almost isotropic within the pitch angle range of 0/180° ± ~12 (half of the angular resolution of the Geotail instrument is 11.25°).

[25] Figure 5 shows the orbital coverage (the leftmost panels) and average PSDs of mirroring O$^+$ with these five energies at FAST altitudes (i.e., whose pitch angle a is around 90°) in each MLT-ILAT bin (the rest of panels) for the FAST-1 (Figure 5a) and FAST-2 (Figure 5b) data set. As shown in the leftmost panels of Figure 5, the data coverage of these data sets is good in the dayside regions around the cusp but poor in the nightside. In the following we will concentrate only in the dayside regions, which are the most likely source regions of COBs in the lobe/mantle. As shown in Table 2, occurrence frequency of mirroring O$^+$ observations tends to increase with energy. FAST observed polar cap regions more frequently during FAST-2 interval than during the FAST-1 intervals, which causes the occurrence frequency difference between FAST-1 and FAST-2 data sets. It should be noted that in all conditions the occurrence frequency of mirroring O$^+$ observations is larger than the average detection probability of COBs in the lobe/mantle (~13% [*Seki et al.*, 1999]).

[26] Going from the 500 eV to the 10 keV panel in each row of Figure 5, the O$^+$ PSDs decrease gradually with increasing energy on average. In each energy, low-altitude mirroring is observed almost everywhere in low-latitude regions, and the O$^+$ PSDs tend to decrease with increasing latitudes except for those at energy 500 eV during low solar activity period (Figure 5a) where there is

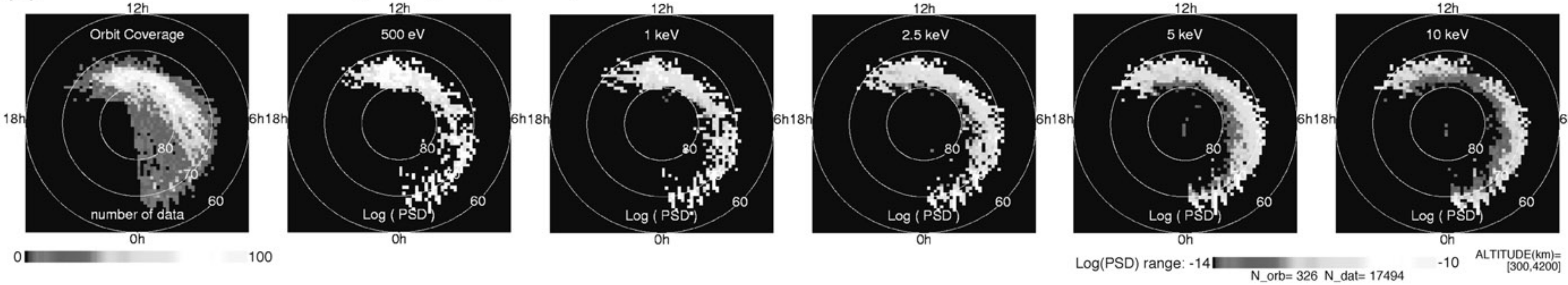

(a) O^+ PSDs observed in the northern polar regions by FAST (11/15/1996 - 1/11/1997: ***FAST1*** data set)

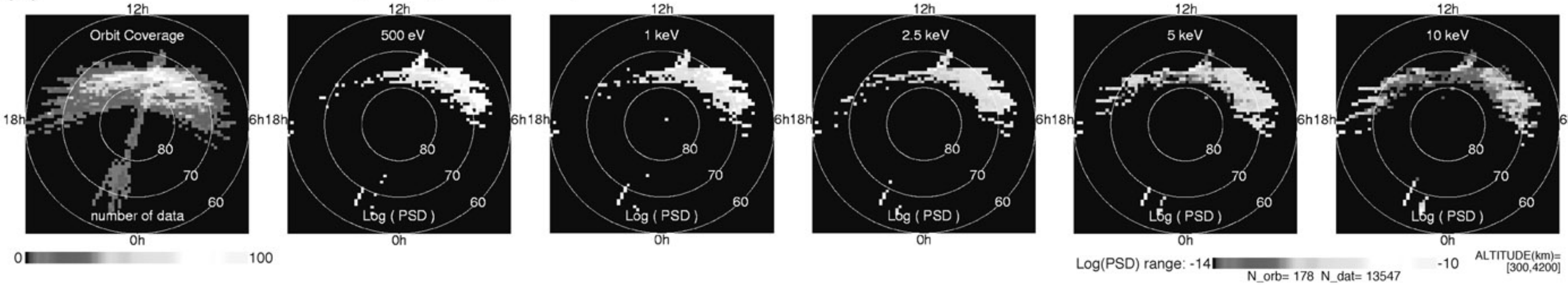

(b) O^+ PSDs observed in the northern polar regions by FAST (11/14/1998 - 2/13/1999: ***FAST2*** data set)

Figure 5. O^+ Observations in northern polar regions by FAST during a low and high solar activity period noted as (a) FAST-1 and (b) FAST-2 in Figure 3 and the text. The radial distance from the center of each panel represents the ILAT, and the clock angle corresponds to the MLT. With color codes the number of data in each MLT-ILAT bin is shown in the leftmost panels, and the averages of O^+ PSD in each MLT-ILAT bin are displayed in the rest of panels. See color version of this figure at back of this issue.

some enhancement near the cusp. The enhancement at the low energy is probably due to perpendicular heating around the cusp region (i.e., fluxes due to local conic production rather than to mirroring magnetospheric fluxes). The lack of the cusp enhancement for the high solar activity data set (Figure 5b) at 500 eV is because of the elimination of high proton count data (pure cusp) described in section 2 in which contamination from proton to the heavy ions is not negligible.

[27] In order to clarify the dependence on the solar activity the PSD ratios of FAST-2 to FAST-1 are summarized in Table 3. When we compare observations in the whole dayside, the O^+ PDSs increased by a factor of $\sim$3–4.6 with an increase in $F_{10.7}$ by a factor of 1.87. The rise becomes smaller for the limited MLT range around the cusp: $\sim$2.4–3.8. These results are consistent with previous studies that showed an increase of O^+ populations with $F_{10.7}$ in the ring current and the polar outflows, as mentioned in section 1. Since the solar activity for the Geotail data set is in the middle of these two FAST data sets, O^+ PSDs both for FAST-1 and FAST-2 will be compared with those of COBs in the lobe/mantle in section 4.3.

4.3. Statistical Comparison of O^+ Populations Observed by FAST and Geotail

[28] When the PSD of O^+ ions whose pitch angle at FAST, θ_F, is 90° is traced to the Geotail position in the lobe/mantle, it will move along a constant energy surface, reducing its pitch angle to θ_G, which satisfies $\sin^2 \theta_G = B_G/B_F$, assuming adiabatic motion, i.e., no energization between FAST and Geotail locations. When we add the "gradual" energy gain due to the drift motion in the magnetosphere discussed in section 3, the particle will gradually move to the higher-energy surface, and the change in pitch angle will become slower than the no energization case. Using this features, we will compare the PSDs of COBs in the lobe/mantle with those of mirroring O^+ in the low-altitude polar regions. Practically, θ_G obtained from the difference of the MGF strength between Geotail and FAST is typically a few degrees and much less than the angular resolution of the Geotail instrument. Thus we assume that the PSD of O^+ mirroring at FAST moves into an angular bin including the peak PSD of COBs at Geotail, and these two PSDs will be compared statistically using the data sets GEOTAIL, FAST-1, and FAST-2.

[29] For the statistical comparison, five energies at FAST, i.e., 0.5, 1, 2.5, 5, and 10 keV, are selected. From the estimation of the minimum energy gain shown in Table 1, correspondent energies for Geotail are 0.64, 1.19, 2.81, 5.43, and 10.59 keV. Figure 6 shows the histograms of O^+ PSDs at these five energies from top to bottom. The green shaded bars in each panel displays the distribution of peak PSDs of COBs observed by Geotail. As expected from the energy distribution of the average peak PSD shown in Figure 4b, the PSD distributions shown with green bars move to lower PSD values with increasing energies, and the decreasing rate from 640 eV to 1.19 keV is the highest. Together with the green histogram, the histogram of PSDs observed by FAST is also plotted Figures 6a–6j. The black, blue, and red bars show observations in all MTL, dayside ($6 \leq \mathrm{MTL} \leq 18$), and near-cusp ($10.5 \leq \mathrm{MTL} \leq 13.5$), respectively. Figures 6a–6e correspond to the FAST-1 data set in a period of low solar activity, while Figures 6f–6j display the FAST-2 data set observed in a period of high solar activity period. When we compare the blue histograms, we can see that PSDs of O^+ at FAST during the high solar activity period are larger than those during the low solar activity period. This difference becomes smaller for red histograms, which only show the data of limited MTL range around the cusp as expected from Table 3.

Table 2. Observational Probability of Mirroring O^+ in Dayside (MLT: 6–18)

	Energy. keV				
	0.5	1.0	2.5	5.0	10.0
FAST-1, %	26.7	25.7	29.5	43.2	45.3
FAST-2, %	15.5	16.9	17.6	23.0	26.9

Table 3. PSD Ratio (FAST-2/FAST-1)

	Energy, keV				
	0.5	1.0	2.5	5.0	10.0
Dayside	3.82	4.06	4.64	3.93	3.01
MLT: 10.5–13.5	2.88	3.42	3.83	3.31	2.43

[30] Now let us compare O^+ PSDs observed in the dayside polar regions with those in the lobe/mantle by comparing blue and red histograms with the green histograms in Figure 6. It should be noted that the ratio of the average $F_{10.7}$ index for GEOTAIL (86.9), FAST-1 (74.6), and FAST-2 (139.8) data sets is 1:0.86:1.61, and the solar activity during the deep tail survey by Geotail is between FAST-1 and FAST-2 and a little closer to FAST-1. As shown in Figures 6h, 6i, and 6j, the green histograms are located below the peak PSDs of the red and blue histograms in the high energies of 2.5–10 keV for the high solar activity period. As for energies of 1 keV of FAST-2 and 5–10 keV of FAST-1, the COB PSD distribution is almost the same as or a little higher than the peak of mirroring O^+ ions (Figures 6d–6e and 6g). These features suggest that statistically, there exist adequate O^+ ions in the dayside magnetosphere to supply high-energy COBs in the lobe/mantle if these trapped O^+ can remain in the magnetosphere after a field line becomes open via dayside reconnection.

[31] To the contrary, the peak of the COB PSD distribution at energy of 640 eV is located at a higher PSD value than the peaks of PSD distributions observed by FAST regardless of solar activity (Figures 6a and 6f). This features seems to be consistent with an inference made in section 4.1 that there is more than one source of COBs, depending on energy. Solid diamonds in Figure 7 show the distribution of average peak PSDs of COBs, which was already shown in Figure 4. Together with the COB distribution, the averages of PSD distributions observed by FAST around the cusp, i.e., in a MTL range of [10.5, 13.5], are displayed with error bars that represent the standard deviation of distribution. Open circles and lightly shaded bars in Figure 7 correspond to the FAST-1 the data set of low solar activity, while open squares and darkly shaded bars correspond to the FAST-2 data set of high solar activity. As shown the PSDs during the period of the high solar activity are larger than those during the period of low solar activity. This dependence on solar activity becomes smaller with increasing energy. These results suggest that the trapped O^+ in the dayside magnetosphere can be a potential source of COBs at energies above $\sim$1 keV. As for the COBs below $\sim$1 keV, on the other hand, the trapped ions cannot be a main contributor without energization. For further interpretation of these results we need to know how much of the O^+ on closed flux tubes can remain in the magnetosphere after the dayside reconnection.

5. Discussion

[32] In this paper the origin of COBs observed in the lobe/mantle regions of the Earth's magnetosphere is investigated on the basis of comparison of the FAST and Geotail data utilizing trajectory tracings in magnetosphere models. In this section we will reconsider the plasma supply mechanisms to the lobe/mantle regions. Let us begin by reviewing the conventional view before the Geotail mission, which carried out a systematic survey of the magnetotail over a wide range of tailward distance up to 210 R_E with a comprehensive set of plasma instruments including ion detectors. As illustrated in Figure 8a, there are two primary sources of the lobe/mantle plasmas, i.e., plasma entering from the magnetosheath (green) and plasma outflowing from the polar ionosphere

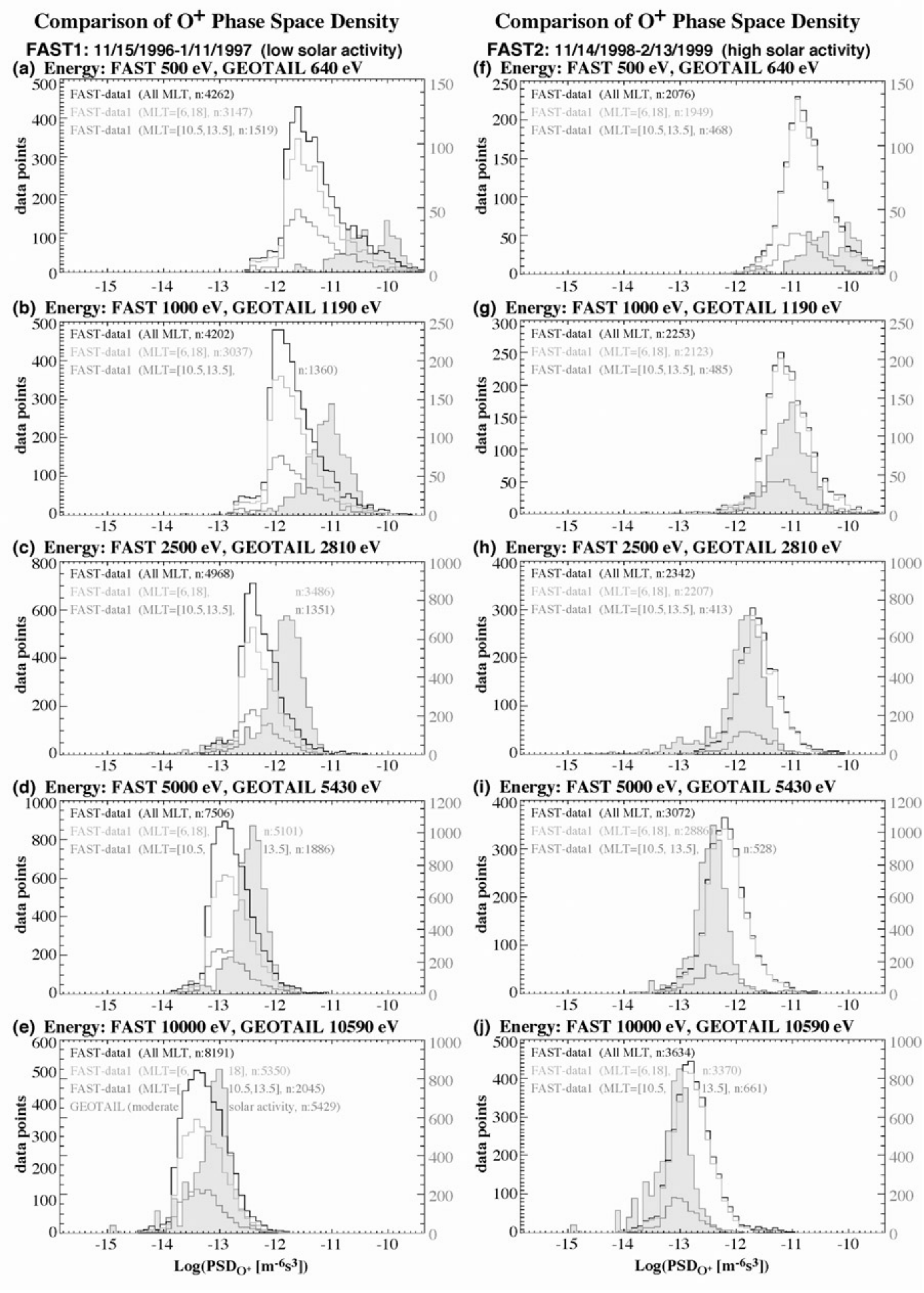

Figure 6. Distribution of O^+ PSD at energies of (a) and (f) 500(640) eV, (b) and (g) 1.00(1.19) keV, (c) and (h) 2.50(2.81) keV, (d) and (i) 5.00(5.43) keV, and (e) and (j) 10.00(10.59) keV for FAST(Geotail) data sets. The green histogram in each panel displays the peak PSD distribution of COBs observed by Geotail. FAST observations are shown with black (all MLT), blue (dayside), and red (near-cusp). Figures 6a–6e correspond to the low solar activity period of the FAST-1 data set, and Figures 6f–6j correspond to the high solar activity of the FAST-2 data set. See color version of this figure at back of this issue.

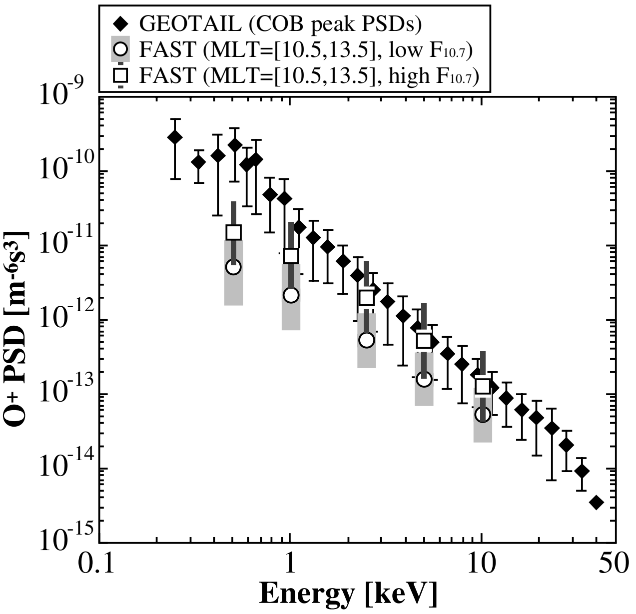

Figure 7. Peak locations of PSD distributions of mirroring O^+ ions for MLT between 10.5 and 13.5 hours are plotted against energy with error bars that display their half width. Open circles and lightly shaded bars correspond to the low solar activity period (FAST-1) while the open squares and darkly shaded bars correspond to the high solar activity period (FAST-2). For comparison, averages of COB peak PSDs, which are already shown in Figure 4, are also shown with solid diamonds.

(rose). The former source, the magnetosheath plasma, is considered to have entered through the cusp region in the dayside magnetosphere and subsequently converted toward the tail region after mirroring in the stronger magnetic field at low altitudes [*Rosenbauer et al.*, 1975]. During periods of southward IMF, magnetosheath plasma can enter not only from the cusp but also almost continuously along the "open" magnetopause, where the normal component of the local MGF is nonzero [*Zwickl et al.*, 1984]. These plasmas entering from the magnetosheath from a boundary layer referred to as the plasma mantle where the plasma parameter change gradually from the outside sheath value to the inside lobe values [*Akinrimisi et al.*, 1990; *Siscoe et al.*, 1994]. If the B_y component of IMF is strong, the motion of magnetic flux tubes reconnected at the dayside magnetopause is expected to cause a dawn-dusk and north-south plasma asymmetry in the magnetotail [*Gosling et al.*, 1985] (see also Figure 8a, which illustrates the positive IMF B_y case). The plasma asymmetry can be seen statistically in Geotail observations.

[33] Ionospheric polar outflow is also considered to be an important contributor to the lobe/mantle plasma [e.g., *Chappell et al.*, 1987] The ions flowing out from the polar ionosphere as (UFI) conics and beams [*Kondo et al.*, 1990], cleft ion fountain [*Lockwood et al.*, 1985], and polar wind [*Abe et al.*, 1993] will enter the plasma mantle and/or the lobe regions on their way to the plasma sheet because of magnetospheric convection. Observations at low altitudes by polar orbiting satellites have shown that the ionospheric ion outflows typically have energies below 1 keV [*Yau and André*, 1997, and references therein]. From a typical outflowing energy and a typical magnitude of the magnetospheric convection these ionospheric ions are considered to be injected into the plasma sheet in the near-Earth region and are not able to reach the distant lobe/mantle. However, Geotail has observed heavy ionospheric ion (O^+ and He^+) beams flowing tailward in the mantlelike regions over a wide range of distance up to 210 R_E, and hence we need a comprehensive view that can also explain supply mechanisms of these ionospheric ions. It should be noted that Geotail can observed O^+ beams above ~250 eV, while cold ions below the energy are also important to discuss the net O^+ content in the magnetosphere [*Seki et al.*, 2001]. According to the statistical properties of cold O^+ beams (COBs) [*Seki et al.*, 1998a] the average energy of the COBs is much higher than the typical energy of polar ionospheric outflows as mentioned above. *Seki et al.* [1998a] have proposed three candidates of the supply scenario of COBs to the distant tail: (1) Extra energization of dayside polar ionospheric outflows, (2) circulation of energetic UFI beams generated mainly around the nightside auroral zone, and (3) release of trapped ions in the dayside magnetosphere by the dayside reconnection.

[34] As for the first candidate, quantitative comparison of COBs with polar O^+ outflows shows that the O^+ ions need to be accelerated up to ~2.7 keV on average if they are the main contributor to the COBs in the distant tail [*Seki et al.*, 1998b]. From the alternating occurrence and density anticorrelation between O^+ and He^+ on a short timescale the acceleration is most likely due to mechanisms leading to a different velocity for different ion species, unless there are mechanism that enhance source fluxes of O^+ and He^+ exclusively to each other [*Seki et al.*, 1999]. According to our knowledge, any evidence for this kind of acceleration such as a parallel potential drop in the high-altitude cusp region has not been reported yet, while there is a recent report on the significant centrifugal acceleration up to several keV just after arrival of a large-pressure pulse in the solar wind [*Moore et al.*, 1999]. We do not intend to exclude the possibility that centrifugal acceleration, which leads to the same velocity for different ion species, is responsible for bringing the cusp/cleft originating ions to the distant lobe/mantle during a period of unusual changes in the convection electric field such as that due to the arrival of a large solar wind pressure pulse. However, such a large pressure pulse, which can push the subsolar magnetopause to geosynchronous orbit and accelerate O^+ ions up to 10 keV or so, is not as frequent as the COB detection in the distant lobe/mantle. On the other hand, the distribution of the averaged peak phase space density shown in Figure 4b suggests that more than one source contributes to the COBs and that one of the sources is primarily <1 keV and that its typical energy is around 500 eV. Since these low-energy COBs are primarily observed in the near-Earth regions, the COBs below 1 keV most likely come from the polar ionospheric O^+ outflows that are convected into the near-Earth lobe/mantle before being injected into plasma sheet. These observation of low-energy COBs are consistent with the conventional view, as mentioned above. For the possibility of other extra energization leading to different velocities for different ion species, observations in the high-altitude cusp region by such spacecraft as Polar, Interball, and Cluster II will be important.

[35] As for high-energy COBs above 1 keV, the validity of the second and third candidates also needs to be investigated quantitatively. The comparison of the O^+ PSD observed by FAST and Geotail reported in this paper has revealed that the PSD of mirroring O^+ at FAST altitudes in dayside is comparable in quantity to that of high-energy COBs above 1 keV. These results suggest that the trapped O^+ in the dayside magnetosphere can be a source of COBs at energies above 1 keV if the O^+ ions trapped in the closed regions can remain in the magnetosphere after the flux tube becomes open via the dayside reconnection. Since the altitude of FAST observations ranges from 300 to 4200 km, FAST can only observe a limited part of the trapped ions, and the pitch angle range of FAST observations corresponds to a few degrees around 0° or 180° in the equatorial region. Thus we cannot tell whether the O^+ observed by FAST is a part of an isotropic distribution or of a beam distribution in the equatorial plane. In other words, it is difficult to distinguish the second and third from the FAST observations.

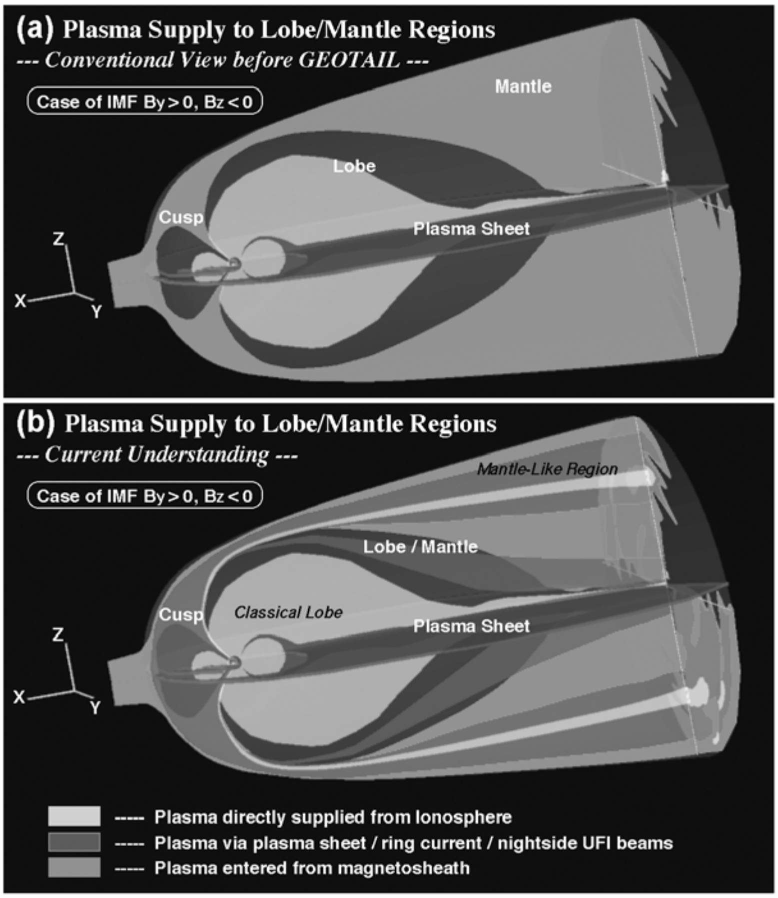

Figure 8. (a) A conventional view before the deep tail survey by Geotail and (b) current understanding of plasma supply mechanisms to the magnetotail are illustrated schematically for the case of positive IMF B_y and southward IMF B_Z. Figures 8a and 8b illustrate the geomagnetosphere with combination of noon-midnight plane, equatorial plasma sheet, and north-south dawn-dusk plane. As indicated at the bottom of the figure, different colors correspond to plasmas of different origins. In regions where more than one plasma coexist, middle tints between colors corresponding to coexisting plasmas are used: green and light green (solar wind originating plasma), rosy colors (plasma of ionospheric origin), and brown and yellowish colors (high-energy plasma, a mixture of solar wind and ionospheric plasmas). See color version of this figure at back of this issue.

[36] Trajectory tracings of O^+ ions in steady magnetospheric models similar to those used in section 3 provide help for this issue: Calculation of O^+ trajectories initially composing an isotropic distribution on the closed flux tubes in the dayside magnetosphere shows that field-aligned or anti-field-aligned particles have a larger probability of transportation to the lobe mantle than particles whose pitch angles are near 90° (Seki et al., manuscript in preparation, 2002). Their results suggest that the transport rate to the lobe/mantle will increase if the O^+ is forming a field-aligned beam rather than an isotropic distribution, and this favors the second candidate rather than the third. As for the restriction on energization mechanisms from the density anticorrelation of O^+ and He^+ mentioned above [*Seki et al.*, 1999], the second candidate can easily be consistent with it since the UFI beams are accelerated by a parallel potential drop that leads to the same energy for different ion species, i.e., to different O^+ and He^+ velocities. The third candidate, on the other hand, seems to need a spatial inhomogeneity of O^+ and He^+ distributions in the dayside magnetosphere or a difference in bulk velocity between these two ion species to explain the O^+ and He^+ density anticorrelation observed by Geotail. For a definitive conclusion of the relative contribution of the second and third candidates, ion composition measurements in the dayside magnetosphere as well as around the reconnection site will provide a crucial key.

[37] On the basis of discussions presented so far, current understanding of plasma supply to the lobe/mantle regions is summarized in Figure 8b. As shown, new aspects are added by this study to the conventional view, which is illustrated in Figure 8a. Namely, the lobe mantle plasma is considered to have at least the following four supply routes: (1) direct entry of dayside polar ionospheric outflows in the near-Earth regions (rose), (2) plasma entered from the magnetosheath through the magnetopause (green), (3) extra energization of polar outflows by a large pressure pulse and possibly by other mechanisms (rose), and (4) transport of trapped plasma with isotropic and/or beam distributions in the dayside magnetosphere via dayside reconnection (brown).

[38] **Acknowledgments.** We are grateful to the FAST PI Charles W. Carlson and all the ESA and TEAMS teams for the data and software used in this study. The authors specially thank Eric Dors for his extensive effort to build convenient data-processing environment for FAST data at LANL. We would like to also thank all Geotail science members for their collaboration. D. C. Delcourt is greatly acknowledged by the authors for his useful suggestion of the trajectory tracing code. This work was carried out under the auspices of the Research Fellowships of the Japan Society for the Promotion of Science for Young Scientists.

[39] Hiroshi Matsumoto thanks K. Marubashi and T. W. Speser for their assistance in evaluating this paper.

References

Abe, T., B. A. Whalen, A. W. Yau, R. E. Horita, S. Watanabe, and E. Sagawa, EXOS D (Akebono) suprathermal mass spectrometer observations of the polar wind, *J. Geophys. Res.*, *98*, 11,119–11,203, 1993.

Akinrimisi, J., S. Orsini, M. Candidi, and H. Balsiger, Ion dynamics in the plasma mantle, *Ann. Geophys.*, *8*, 739–754, 1990.

Büchner, J., and L. M. Zelenyi, Regular and chaotic charged particle motion in magnetotail-like field reversals, 1, Basic theory of trapped motion, *J. Geophys. Res.*, *94*, 11,821–11,842, 1989.

Carlson, C. W., and J. P. McFadden, Design and applications of imaging plasma instruments, in *Measurement Techniques in Space Plasmas, Geophys. Monogr. Ser.*, vol. 102, edited by J. Borovsky, R. Pfaff, and D. T. Young, pp. 125–140, AGU, Washington, D.C., 1998.

Carlson, C. W., R. F. Pfaff, and J. G. Watzin, The Fast Auroral Snapshot (FAST) mission, *Geophys. Res. Lett.*, *25*, 2013–2016, 1998.

Chappell, C. R., T. E. Moore, and J. H. Waite Jr., The ionsphere as a fully adequate source of plasma for the Earth's magnetosphere, *J. Geophys. Res.*, *92*, 5896–5910, 1987.

Cowley, S. W. H., Plasma populations in a simple open model magnetosphere, *Space Sci. Rev.*, *26*, 217–275, 1980.

Delcourt, D. C., J.-A. Sauvaud, R. F. Martin Jr., and T. E. Moore, On the nonadiabatic precipitation of ions from the near-Earth plasma sheet, *J. Geophys. Res.*, *101*, 17,409–17,418, 1996.

Fairfield, D. H., N. A. Tsyganenko, A. V. Usmanov, and M. V. Malkov, A large magnetosphere magnetic field database, *J. Geophys. Res.*, *99*, 11,319–11,326, 1994.

Gosling, J. T., D. N. Baker, S. J. Bame, W. C. Feldman, R. D. Zwickl, and E. J. Smith, North-south and dawn-dusk plasma asymmetries in the distant tail lobes: ISEE-3, *J. Geophys. Res.*, *90*, 6354–6360, 1985.

Gussenhoven, M. S., D. A. Hardy, N. Heinemann, and R. K. Burkhardt, Morphology of the polar rain, *J. Geophys. Res.*, *89*, 9785–9800, 1984.

Hirahara, M., K. Seki, and T. Mukai, Cold dense ion flows in the distant magnetotail: The Geotail results, in *New Perspectives on the Earth's Magnetotail, Geophys. Monogr. Ser.*, vol. 105, edited by A. Nishida et al., pp. 45–60, AGU, Washington, D.C., 1998.

Kokubun, S., T. Yamamoto, M. H. Acuña, K. Hayashi, K. Shiokawa, and H. Kawano, The geotail magnetic field experiment, *J. Geomagn. Geoelectr.*, *46*, 7–21, 1994.

Kondo, T., B. A. Whalen, A. W. Yau, and W. K. Peterson, Statistical analysis of upflowing ion beam and conic distribution at DE 1 altitudes, *J. Geophys. Res.*, *95*, 12,091–12,102, 1990.

Lockwood, M., J. H. Waite Jr., T. E. Moore, J. F. E. Johnson, and C. R. Chappell, A new source of suprathermal O^+ ions near the dayside polar cap boundary, *J. Geophys. Res.*, *90*, 4099–4116, 1985.

Lyons, L. R., Magnetospheric processes leading to precipitation, *Space Sci. Rev.*, *80*, 109–132, 1997.

Lyons, L. R., and T. W. Speiser, Evidence for current-sheet acceleration in the geomagnetic tail, *J. Geophys. Res.*, *87*, 2276–2286, 1982.

Möbius, E., et al., The 3-D plasma distribution function analyzers with time-of-flight mass discrimination for Clusters, FAST, and Equator-S, in *Measurement Techniques in Space Plasmas: Particles, Geophys. Monogr. Ser.*, vol. 102, edited by J. Borovsky, R. Pfaff, and D. T. Young, pp. 243–248, AGU, Washington, D.C., 1998.

Moore, T. E., W. K. Peterson, C. T. Russell, M. O. Chandler, M. R. Collier, H. L. Collin, P. D. Craven, R. Fitzenreiter, B. L. Giles, and C. J. Pollock, Ionospheric mass ejection in response to a coronal mass ejection, *Geophys. Res. Lett.*, *26*, 2339–2342, 1999.

Mukai, T., S. Machida, Y. Saito, M. Hirahara, T. Terasawa, N. Kaya, T. Obara, M. Ejiri, and A. Nishida, The low energy particle (LEP) experiment onboard Geotail satellite, *J. Geomagn. Geolectr.*, *46*, 669–692, 1994a.

Mukai, T., M. Hirahara, S. Machida, Y. Saito, T. Terasawa, and A. Nishida, Geotail observation of cold ion streams in the medium distance magnetotail lobe in the course of a substorm, *Geophys. Res. Lett.*, *21*, 1023–1026, 1994b.

Newell, P. T., and C.-I. Meng, The cusp and boundary layer: Low-altitude identification and statistical local time variation, *J. Geophys. Res.*, *93*, 14,549–14,556, 1988.

Newell, P. T., and C.-I. Meng, Mapping the dayside ionosphere to the magnetosphere according to particle precipitation characteristics, *Geophys. Res. Lett.*, *19*, 609–612, 1992.

Onsager, T. G., C. A. Kletzing, J. B. Austin, and H. MacKierman, Model of magnetosheath plasma in the magnetosphere, *Geophys. Res. Lett.*, *20*, 479–482, 1993.

Rosenbauer, H., H. Grünwaldt, M. D. Montgomery, G. Paschmann, and N. Sckopke, HOES/2 plasma observations in the distant polar magnetosphere: The plasma mantle, *J. Geophys. Res.*, *80*, 2723–2737, 1975.

Seki, K., M. Hirahara, T. Terasawa, I. Shinohara, T. Mukai, Y. Saito, S. Machida, T. Yamamoto, and S. Kokubun, Coexistence of Earth-origin O^+ and solar wind-origin H^+/He^+ in the distant magnetotail, *Geophys. Res. Lett.*, *23*, 985–988, 1996.

Seki, K., M. Hirahara, T. Terasawa, T. Mukai, Y. Saito, S. Machida, T. Yamamoto, and S. Kokubun, Statistical properties and possible supply mechanisms of tailward cold O^+ beams in the lobe/mantle regions, *J. Geophys. Res.*, *103*, 4477–4490, 1998a.

Seki, K., T. Terasawa, M. Hirahara, and T. Mukai, Quantification of tailward cold O^+ beams in the lobe/mantle regions with Geotail data: Constraints on polar O^+ outflows, *J. Geophys. Res.*, *103*, 29,371–29,381, 1998b.

Seki, K., M. Hirahara, T. Terasawa, T. Mukai, and S. Kokubun, Properties of He^+ beams observed by Geotail in the lobe/mantle regions: Comparisons with O^+ beams, *J. Geophys. Res.*, *104*, 6973–6985, 1999.

Seki, K., M. Hirahara, T. Terasawa, T. Mukai, and S. Kokubun, Origin and dynamics of multicomponent $(H^+/He^{++}/He^+/O^+)$ ion flows in the lobe/mantle regions, *Adv. Space Res.*, *25*(7–8), 1581–1590, 2000a.

Seki, K., R. C. Elphic, M. F. Thomsen, J. Bonnell, E. J. Lund, M. Hirahara, T. Terasawa, and T. Mukai, Cold flowing O^+ beams in the lobe/mantle at Geotail: Does FAST observe the source?, *J. Geophys. Res.*, *105*, 15,931–15,944, 2000b.

Seki, K., R. C. Elphic, M. Hirahara, T. Terasawa, and T. Mukai, On atmospheric loss of oxygen ions from Earth through magnetospheric processes, *Science*, *291*, 1939–1941, 2001.

Sergeev, V. A., G. R. Bikkuzina, and P. T. Newell, Dayside isotropic precipitation of energetic protons, *Ann. Geophys.*, *15*, 1233–1245, 1997.

Siscoe, G. L., L. A. Frank, K. L. Ackerson, and W. R. Paterson, Properties of mantle-like magnetotail boundary layer: Geotail data compared with a mantle model, *Geophys. Res. Lett.*, *21*, 2975–2978, 1994.

Speiser, T. W., Current sheet particle acceleration - Theory and observations for the geomagnetic tail, *Adv. Space Res.*, *4*(2–3), 439–448, 1984.

Terasawa, T., M. Fujimoto, T. Mukai, I. Shinohara, Y. Saito, T. Yamamoto, S. Machilda, S. Kokubun, A. J. Lazarus, J. T. Steinberg, and R. P. Lepping, Solar wind control of density and temperature in the near-Earth plasma sheet: Wind/Geotail collaboration, *Geophys. Res. Lett.*, *24*, 935–938, 1997.

Tsyganenko, N. A., Modeling the Earth's magnetospheric magnetic field confined within a realistic magnetopause, *J. Geophys. Res.*, *100*, 5599–5612, 1995.

Tsyganenko, N. A., and M. Peredo, Analytical models of the magnetic field of disk-shaped current sheets, *J. Geophys. Res.*, *99*, 199–205, 1994.

Tsyganenko, N. A., and M. Stern, Modeling the global magnetic field the large-scale Birkeland current systems, *J. Geophys. Res.*, *101*, 27,187–27,198, 1996.

Weimer, D. R., Models of high-latitude electric potentials derived with a least error fit of spherical harmonic coefficients, *J. Geophys. Res.*, *100*, 19,595–19,607, 1995.

Weimer, D. R., A flexible, IMF-dependent model of high-latitude electric potentials having "space weather" applications, *Geophys. Res. Lett.*, *23*, 2549–2552, 1996.

Winningham, J. D., and W. J. Heikkila, Polar cap auroral electron fluxes observed with Isis 1, *J. Geophys. Res.*, *79*, 949–957, 1974.

Woch, J., and R. Lundin, Magnetosheath plasma precipitation in the polar cusp and its control by the interplanetary magnetic field, *J. Geophys. Res.*, *97*, 1421–1430, 1992.

Yau, A. W., and M. André, Source of ion outflow in the high latitude ionosphere, *Space Sci. Rev.*, *80*, 1–25, 1997.

Young, D. T., H. Balsiger, and J. Geiss, Correlations of magnetospheric ion composition with geomagnetic and solar activity, *J. Geophys. Res.*, *87*, 9077–9096, 1982.

Zwickl, R. D., D. N. Baker, S. J. Bame, W. C. Feldman, J. T. Gosling, E. W. Hones Jr., D. J. McComas, B. T. Tsurutani, and J. A. Slavin, Evolution of Earth's distant magnetotail: ISEE 3 electron plasma results, *J. Geophys. Res.*, *89*, 11,007–11,012, 1984.

J. Bonnell and J. P. McFadden, Space Science Laboratory, University of California, Berkeley, CA 94720, USA. (jbonnell@ssl.berkeley.edu; mcfadden@ssl.berkeley.edu)

R. C. Elphic and M. F. Thomsen, Space and Atmospheric Sciences Group (NIS-1), MS D466, Los Alamos National Laboratory, Los Alamos, NM 87545, USA. (relphic@lanl.gov; mthomsen@lanl.gov)

M. Hirahara, Department of Physics, College of Science, Rikkyo University, 3-34-1 Nishi-Ikebukuro, Toshima, Tokyo 171-8501, Japan. (hirahara@rikkyo.ac.jp)

E. J. Lund, Space Science Center, Morse Hall, University of New Hampshire, Durham, NH 03824, USA. (Eric.Lund@unh.edu)

T. Mukai, Institute of Space and Astronautical Science, 3-1-1 Yoshinodai, Sagamihara, Kanagawa 229-8510, Japan. (mukai@stp.isas.ac.jp)

K. Seki, Integrated Studies Division, Solar Terrestrial Environment Laboratory, Nagoya University, Honohara 3-13, Toyokawa, Aichi 442-8507, Japan. (seki@stelab.nagoya-u.ac.jp)

T. Terasawa, Department of Earth and Planetary Science, Graduate School of Science, University of Tokyo, 7-3-1 Hongo, Bunkyo, Tokyo 113-0033, Japan. (terasawa@eps.s.u-tokyo.ac.jp)

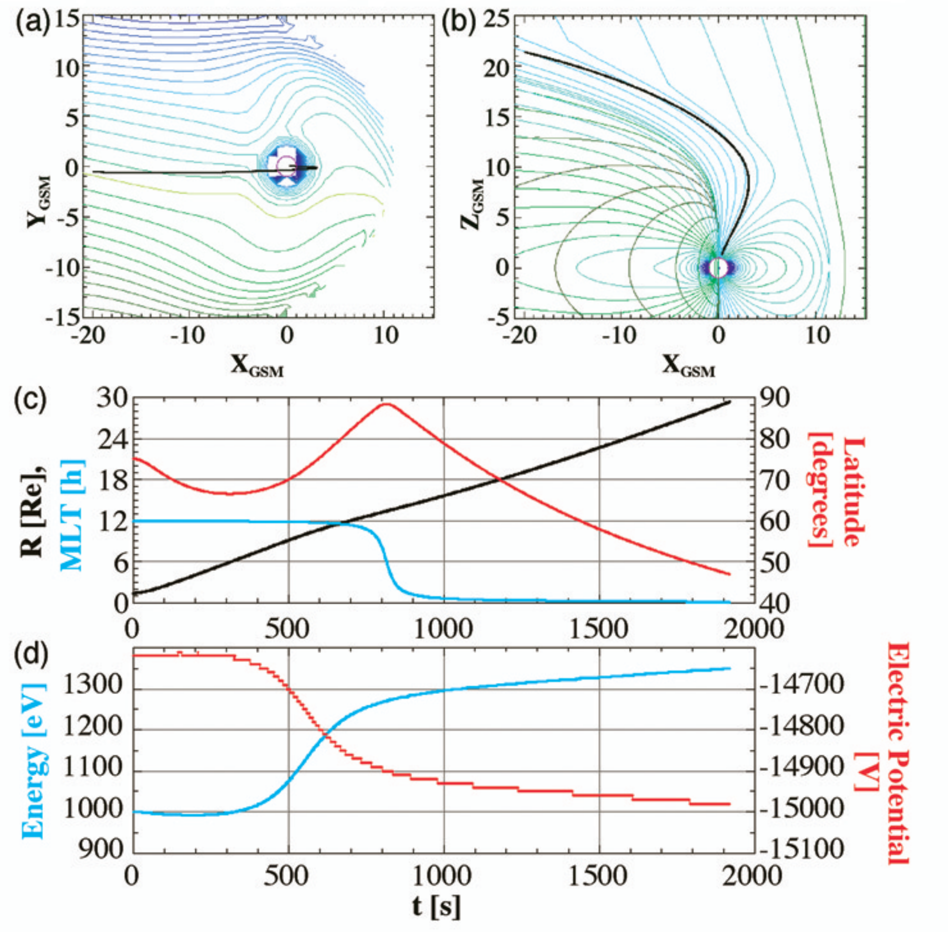

Figure 1. An example of O^+ trajectory in steady empirical magnetospheric models: T96 magnetic field and W96 electric potential models are displayed in GSM coordinates with tilt angle assumed to be zero. Input parameters to the models are dynamic pressure of the solar wind, 2 nPa; the *Dst* index, −100; IMF B_y, 0 nT; IMF B_z; −5 nT; and solar wind velocity, 450 km s^{-1}. (a) The colored lines in panel display electric equipotential lines for each 2.5 kV mapped with T96 model to the equatorial plane. (b) The magnetic fields that have their foot points at MLT = 0, 6, or 12 hours are displayed with colored lines. In each panel the traced O^+ trajectory is shown with the black line. (c) Time variation of particle position with the geocentric distance *R* (black), the MLT (blue), and the latitude (red). The scales for *R* and MLT are the same and are shown on the left-hand side of the panel. (d) The O^+ energy (blue) and local electric potential at the particle position (red).

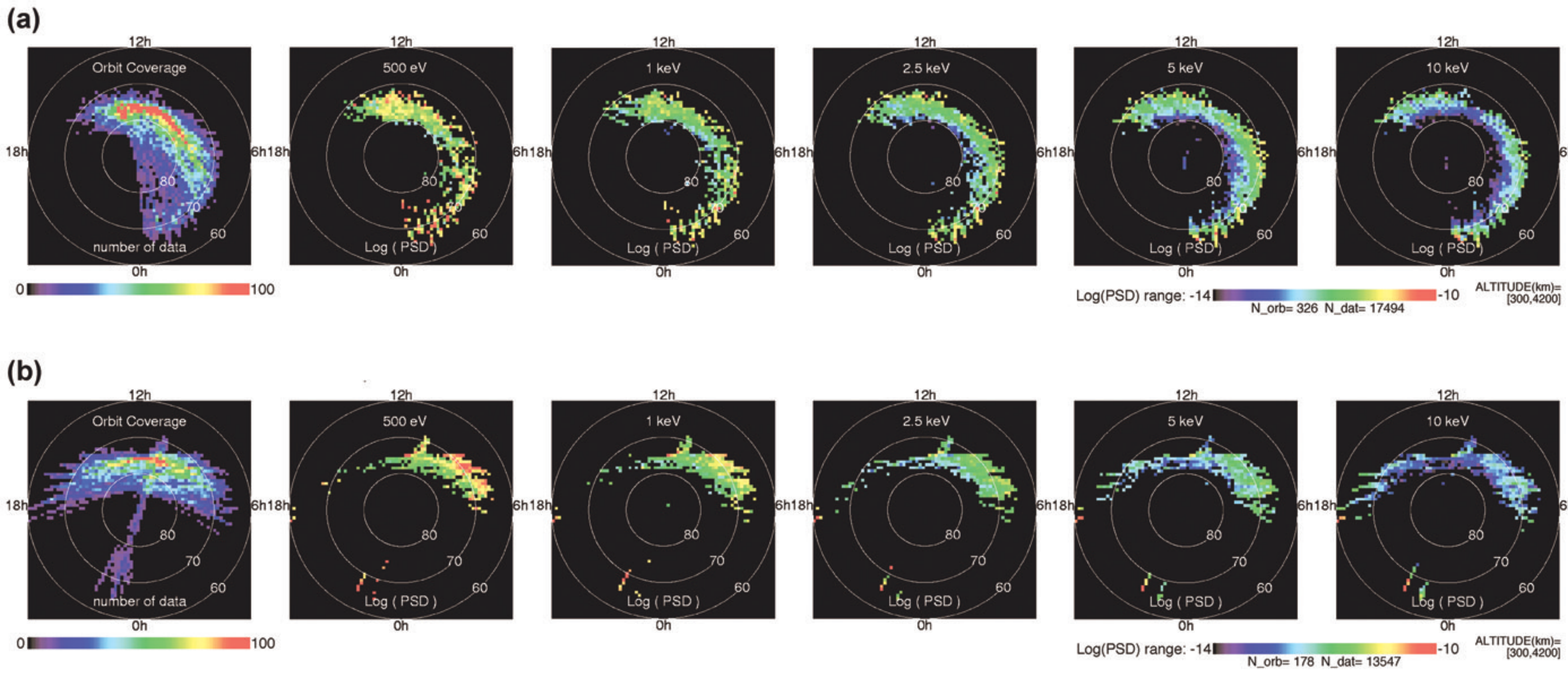

Figure 5. O$^+$ Observations in northern polar regions by FAST during a low and high solar activity period noted as (a) FAST-1 and (b) FAST-2 in Figure 3 and the text. The radial distance from the center of each panel represents the ILAT, and the clock angle corresponds to the MLT. With color codes the number of data in each MLT-ILAT bin is shown in the leftmost panels, and the averages of O$^+$ PSD in each MLT-ILAT bin are displayed in the rest of panels.

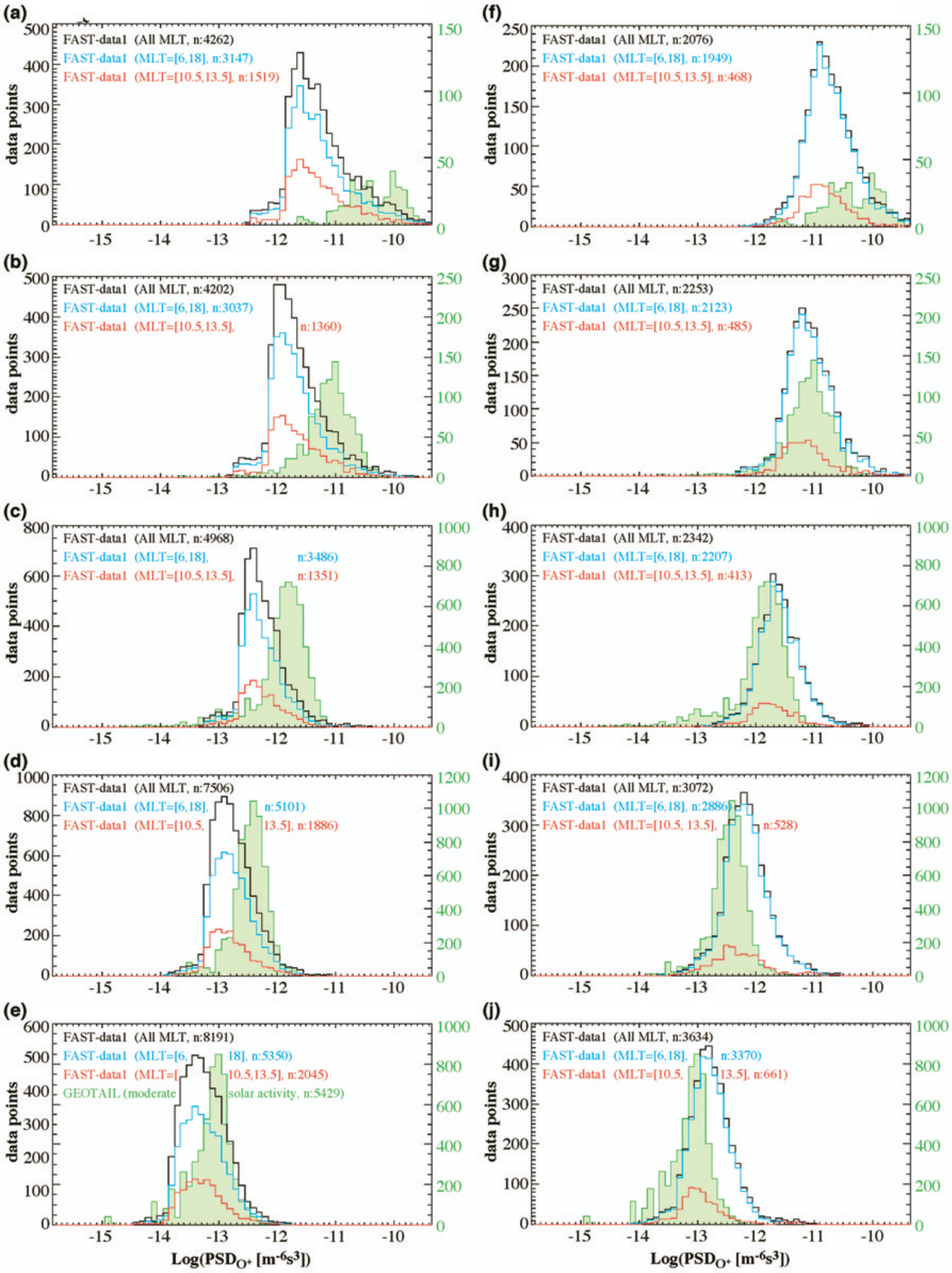

Figure 6. Distribution of O$^+$ PSD at energies of (a) and (f) 500(640) eV, (b) and (g) 1.00(1.19) keV, (c) and (h) 2.50(2.81) keV, (d) and (i) 5.00(5.43) keV, and (e) and (j) 10.00(10.59) keV for FAST(Geotail) data sets. The green histogram in each panel displays the peak PSD distribution of COBs observed by Geotail. FAST observations are shown with black (all MLT), blue (dayside), and red (near-cusp). Figures 6a–6e correspond to the low solar activity period of the FAST-1 data set, and Figures 6f–6j correspond to the high solar activity of the FAST-2 data set.

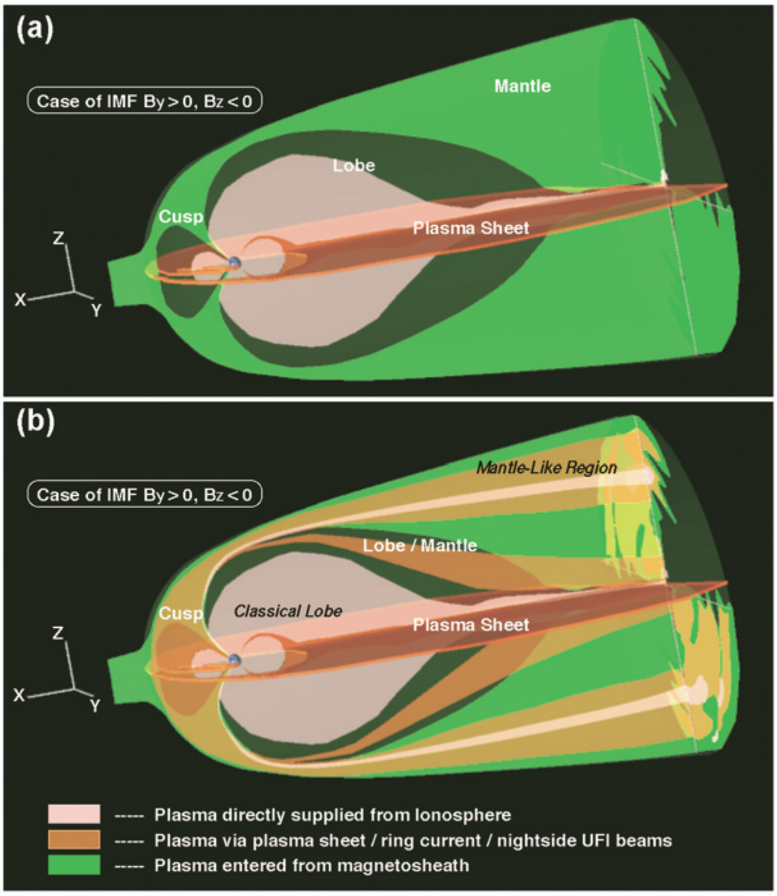

Figure 8. (a) A conventional view before the deep tail survey by Geotail and (b) current understanding of plasma supply mechanisms to the magnetotail are illustrated schematically for the case of positive IMF B_y and southward IMF B_Z. Figures 8a and 8b illustrate the geomagnetosphere with combination of noon-midnight plane, equatorial plasma sheet, and north-south dawn-dusk plane. As indicated at the bottom of the figure, different colors correspond to plasmas of different origins. In regions where more than one plasma coexist, middle tints between colors corresponding to coexisting plasmas are used: green and light green (solar wind originating plasma), rosy colors (plasma of ionospheric origin), and brown and yellowish colors (high-energy plasma, a mixture of solar wind and ionospheric plasmas).